RSC Advances

A Promising Nanocomposite from CNTs and Nano Ceria: Nano-structured Fillers in Polyurethane Coatings for Surface Protection

SCHOLARONE™
Manuscripts

A Promising Nanocomposite from CNTs and Nano Ceria: Nano-structured Fillers in Polyurethane Coatings for Surface Protection

A. Madhan Kumar[*]**, M. Mizanur Rahman and Zuhair M.Gasem**

Center of Research Excellence in Corrosion, Research Institute

King Fahd University of Petroleum and Minerals, Dhahran, Saudi Arabia - 31261

Abstract

The balanced combination of the nanostructured carbon materials and metal oxide nanoparticles has been considered as efficient reinforcement materials in developing the next-generation multifunctional coatings. Herein, we demonstrate a general approach to fabricate a CNT based nanocomposite with the inclusion of CeO_2 nanoparticles that can be effectively implemented as a reinforcement material in surface protective coatings. The synthesized CNT/CeO_2 nanocomposite was characterized by spectral and surface morphological analyses, which indicated that the CeO_2 nanoparticles were successfully deposited onto the surface of CNTs. The XRD pattern shows the semi-crystalline nature of CNTs and the face centered cubic structure of CeO_2 nanoparticles. The prepared nanocomposite has subsequently been used as nanofillers in polyurethane (PU) coatings for surface protection of steel substrates and remarkably synergistic effect of nano ceria and CNT has been observed. The corrosion resistance of the steel coated by PU coating containing CNT/CeO_2 was pointedly higher than that of pure PU coating and PU coating with CNTs alone. This result suggests a new prospect for solving the corrosion issues encountered at the steel structures in the industrial applications using multifunctional hybrid coatings with nanostructured reinforcements.

Keywords: CNTs; Nano-Ceria; Corrosion; Nanocomposite; EIS

[*] **Corresponding author:**

Email: madhankumar@kfupm.edu.sa   Phone: +966538801789

Introduction

The improvement of reinforcement materials has opened a boundless potential for utilization to ripen new generations of materials with multifunctional features. Wide variety of nano-scale reinforcement materials are employed in modern composite materials, among which are elementary and common fillers like titania, alumina, and silica, clays and then carbon nanotubes (CNTs) in single and multiwalled configurations [1-3]. In recent years, the practice of CNTs as a reinforcement material has been given substantial interest due to their remarkable features of a large specific surface area, and hollow and layered structures with excellent physical and mechanical properties. In the past few decades, much effort has been devoted to the improvement of CNTs performance in several applications[4]. In recent times, the decoration of CNT surface with different types of nanoparticles has fascinated significant attraction, since it delivers a new class of multifunctional hybrid materials[5].

Owing to their prospective applications, rare earth materials have attained important consideration and have been investigated for numerous technological applications, such as energy enhancement, biosensors and biomolecule detection, magnets, semiconductor devices and lithium ion batteries[6]. Among the various types of rare earth metal oxides, CeO_2 nanoparticles have received great attention due to their unique catalytic, electrical, and optic properties, as well as their extensive applications in diverse areas[7]. Above all, it plays a crucial role in protective coatings as effective anticorrosion nano fillers[8]. M. Fedel et al have recently reported that the fundamental mechanisms for the behavior of cerium oxides nanoparticles as corrosion inhibitors for steel and suggested that cerium oxide affects the electrochemical properties of mild steel surface; they promoted an ennoblement effect and strong modifications in the impedance response[9]. Thus, combining the advantages of the above mentioned two materials would be favorable to make ideal comprehensive performance for the nanostructured multifunctional coatings in industrial applications.

Recently, CNTs-based metal oxide nanocomposites have drawn more consideration owing to their synergistic contribution of two or more functional constituents in many potential applications. G. V. Pham et al have prepared the Fe_3O_4/CNTs composite with magnetic property by attaching magnetic nanoparticles (Fe_3O_4) to carbon nanotubes (CNTs) and utilized this nanocomposite as nanofiller for epoxy coating for corrosion protection of carbon steel[10]. X.H. Chen et al. have prepared the Ni – carbon nanotube (CNTs) composite coatings on carbon steel and their results suggested that the addition of CNTs in the deposition process of nickel significantly increased the resistance to corrosion[11]. B.M. Praveen et al. have reported that Zn–carbon nanotubes composite coatings from a sulphate bath containing dispersed carbon nanotubes (CNTs) and their study highlights the use of nanofillers for the control of zinc coating corrosion and the electrolyte could be used to generate zinc–CNTs composite coating in plating industry [12].

Huige Wei et al have recently fabricated the polyurethane (PU) nanocomposite coatings filled with CNTs for corrosion prevention of stainless steel and their results indicate that the PU matrix combined with the well dispersed CNT reinforcements provided a significant physical barrier against corrosion[13]. It has been already proved that PU coatings can be considered as a

coating material for corrosion protection of metals due to have sufficient adhesive strength, mechanical strength and barrier resistance under ambient conditions, under moderately high temperatures, and in water. To the best of our knowledge, the nanocomposite fabricated at this juncture implies the first execution of CNTs and nano-ceria in such a surface coating application. In the current investigation, we are mainly focusing on interaction of nano sized ceria particles with functionalized CNTs in terms of nano fillers in responsible for resulting corrosion protection efficiency parameters with varied concentration.

2. Experimental Procedures

2.1 Materials and methods

Ammonium Ce (IV) nitrate, sodium hydroxide (NaOH), Cetyl trimethylammonium bromide (CTAB) and other chemicals used in this study were analytical grades purchased from Aldrich chemical company. The MWCNTs were purchased from Nanotech Port Co. Ltd. (Shenzhen, China) with the following characteristics: 95% purity, 10-15 nm diameter and 1-5 μm length. In order to improve the dispersion of MWCNTs and enhance the interfacial affinity between MWCNTs and CeO_2 nanoparticles, the MWCNTs were oxidized and shortened by stirring with H_2SO_4/HNO_3 (3:1) at 80 ºC for 24 h. The reaction mixture was cooled to room temperature and filtered through a PVDF membrane. The remaining black solid was washed with deionized water (pH=7) and dried for 48 h under vacuum at 60 ºC, giving the functionalized MWCNTs (*f*-CNTs). Aqueous electrolytes used for the synthesis of the nanoparticles and nanocomposite were prepared using double distilled water.

Mild steel (MS) substrates with the following chemical composition were used in the experiments (wt. %): C, 0.15; Mn, 1.26; V, 0.017; Si, 0.035; S, 0.008; Cr, 0.036; Ni, 0.03; Al, 0.083; Cu, 0.038; balance Fe. These substrates were abraded with silicon carbide abrasive paper ranging from grit size 320 to 1200, rinsed with distilled water, placed in an ultrasonic acetone bath for about 5 min. to remove probable residue of polishing, rinsed with acetone, dried in warm air. Prior to each experiment, MS substrates were treated as described and freshly used with no further storage.

2.2. Synthesis of CeO_2 nanoparticles

To synthesize ceria (CeO_2) nanoparticles, the precursors, ammonium Ce (IV) nitrate and NaOH with 1:4 molar ratio were dissolved completely in de-ionized water and the pH value of the solution was adjusted to be 12. The mixture solution was stirred well using a magnetic stirrer for about 2 h and then, the prepared mixture solution was kept in the microwave oven at a temperature of 60 °C for about 1 h. Synthesized pale-yellow precipitate was filtered and washed with de-ionized water twice. Annealing of the synthesized powder at 130 °C in air for 4 h will result in the formation of CeO_2 nanoparticles.

2.3. Synthesis of CNT/CeO_2 nanocomposite

The synthesis procedure of CNT/CeO_2 nanocomposite adopted in the present study is as follows. In the first step, 100 mg of *f*-CNT was dispersed in 100 mL of de-ionized water using an ultrasonicator. Then, aqueous solution of CeO_2 nanoparticles

(2wt. %) containing 0.1 g of CTAB was added slowly to the above-prepared solution of f-CNT, forming a uniform solution on vigorous magnetic stirring. The resulting solution was vigorously stirred at 90 ° C for 8 h. The obtained product was washed several times using de-ionized water and ethanol, and dried at 60 °C in a vacuum overnight. Finally, a black powder was obtained and labeled as CNT/CeO$_2$.

The MS substrates which were previously pretreated in acetone and then, 0.5, 1 and 2 Wt.% of CNT/CeO$_2$ were dispersed in acetone using an ultra-sonication for about 1h and coated using polyurethane matrix (HDI biuret polyisocyanate, viscosity is 0.17–0.24 mPa s, content of –NCO is 16.5 ± 1%), through dipping method and denoted as PU-CNT/Ce1, PU-CNT/Ce2 and PU-CNT/Ce3, respectively. In order to apply an equal coating thickness on the MS substrates, the time of dipping in coating bath was similar for all the synthesis conditions. The duration of dipping process was 1 min (including immersing and eliciting). Subsequently, the coated substrates were dried in oven at the temperature of 60 °C for 18 h. For the sake of comparison, pure polyurethane (PU) and polyurethane with 2 Wt. % of f-CNTs (PU/CNT) were also prepared in the same condition as mentioned above.

2.4 Characterization of synthesized CNT/CeO$_2$ nanocomposite

The CNT/CeO$_2$ hybrid nanocomposite was characterized by UV-visible spectroscopy (Shimadzu UV-2100 spectrometer) in the range 200–800 nm. IR spectra for the synthesized nanocomposite were recorded in the range of 400-4000 cm^{-1} using IR reflectance spectrophotometry (PerkinElmer, Spectrum One, with universal ATR attachment with a diamond and ZnSe crystal, The Netherlands) to confirm the formation of nanocomposite. The crystalline features of the synthesized products were examined through powder X-ray diffraction (XRD) using a Rigaku Corporation, Tokyo, Japan. The spectra were recorded at room temperature over a scattering angle range of $20° \leq 2\Theta \leq 80°$ at a 2Θ step of 0.02°. Raman spectral analysis was performed using Yvon Jobin Horiba Raman spectrometer with the spectrum window of 200–2000 cm^{-1} through green type laser source at 532 nm. Thermal degradation of the CNT nanocomposite was performed using a thermogravimetric analyzer (TA instruments, TGA 50). The thermal experiment consisted of a thermal scan at a velocity of 10 °C min^{-1} from 30 °C up to 1000 °C in nitrogen atmosphere.

The surface morphology of the synthesized products was analyzed using scanning electron microscope (SEM); JSM-6360 (JEOL), at an acceleration voltage of 20 kV and irradiation current of 10 μA. The associated energy dispersive X-ray analyzer (EDAX) has provided qualitative information about surface elemental composition. TEM measurements were taken using a Hitachi H-600 transmission electron microscope. For TEM observation, synthesized CNT/CeO$_2$ nanocomposite was suspended in ethanol and a drop of the dispersion was placed onto a carbon film supported by a copper grid.

Contact angles of the substrates were measured by contact angle goniometry at 25 °C using an Attension optical goniometer interfaced with image-capture software by introducing a 2 μL liquid drop. Deionized water was used as the test

liquid. The standard deviation of contact angle measurements is about ± 0.1°. To acquire reliable contact angle data, five droplets were dispensed at different regions of the uncoated and coated MS substrates.

2.5. Electrochemical Corrosion studies

All electrochemical corrosion investigations were performed in a one-compartment cell with three electrodes connected to Gamry Instrument potentiostat/galvanostat/ZRA (Reference 3000) with a Gamry framework system based on ESA410. The MS substrates were the working electrode; platinum wire was used as the counter electrode and saturated calomel electrode (SCE) as the reference electrode and all potentials were measured versus the SCE reference electrode. Tafel curves were obtained by changing the electrode potential automatically from −250 to +250 mV versus the open-circuit potential (OCP) at a scan rate of 1 mV s^{-1}. EIS measurements were carried out under potentiostatic conditions in a frequency range from 100 kHz to 100 mHz, with an amplitude of 10 mV, using an alternating-current signal at OCP. All experiments were measured after immersion for 30 min. in 3.5% NaCl solution. The analysis of the impedance spectra was evaluated by fitting the experimental results to equivalent circuits using the non-linear least-square fitting procedure. All measurements were repeated at least three times until good reproducibility of the results was obtained.

Results and Discussions

3.1 Structural characterization

Figure 1a displays the IR spectra of the functionalized CNTs, synthesized nano-ceria and their nanocomposite. The pristine CNTs display typical weak peaks of C = C aromatic ring stretching at the wavenumber of around 1600 cm^{-1} (Fig. S1). After functionalization, the presence of the band at 1602 cm^{-1} and broad shoulder band in the 3200-3600 cm^{-1} region are evidently consigned to the stretching mode of carboxyl and hydroxyl groups, indicating the presence of –COOH and –OH on the surfaces of f-CNTs[14]. The strong band in the low wavenumber region around 600–500 cm^{-1} is due to characteristic Ce–O vibrations[15]. IR curve of CNT/CeO$_2$ nanocomposite indicates that it has appropriate peaks from both the CeO$_2$ nanoparticles and the CNTs. Further, few peaks of CNT in the IR curve of nanocomposite were moved to lower wavenumber, which possibly caused by the interaction between the CeO$_2$ nanoparticles and CNTs through the formation of hydrogen bonding between hydroxyl group from the walls of the CNT surface and oxygen of CeO$_2$ [16, 17].

The UV-Vis spectra taken for the functionalized CNTs, synthesized nano-ceria and their nanocomposite are shown in Fig. 1b. It can be shown that the functionalized CNT samples produce no absorption peaks in the range of 200–800 nm[18]. In the case of pure CeO$_2$ nanoparticles, the peak appeared at around 300 nm corresponds to the characteristic absorption of nano-ceria[19]. The appearance of this peak at 308 nm in nanocomposite confirms the formation of CNT/CeO$_2$ nanocomposite. Further, the shifting of peak towards the higher wavelength (red shift) which is ascribed to the interaction between CeO$_2$ and f-CNTs.

6

Fig. 2a displays the X-ray diffractograms of f-CNTs, with a characteristic reflection appear at $2\Theta = 25.8$ and $43.6°$ corresponding to (002) and (100) reflections of the conjugated graphitic systems, indicative of an approximately intact hexagonal graphite structure of CNTs [20]. It can be seen that the as-synthesized CeO_2 and the CNT/CeO_2 nanocomposite presented very similar XRD patterns, however with slight differences in the intensities of the diffraction peaks. The XRD patterns of CNT/CeO_2 nanocomposite exhibited four major peaks at 28.7, 33.2, 47.7, and 56.5, which are correspondingly related to (111), (200), (220), and (311) planes of face-center cubic CeO_2 (JCPDS 78-0694). Using Debye–Scherrer's equation, average crystalline sizes of cerium nanocrystals in CNT/CeO_2 were found to be about 12-15 nm. Disappearance of the reflection planes at (002) and (100) in the CNT/CeO_2 nanocomposite is attributed to the low degree of graphitization caused by the deposition of CeO_2 nanoparticles on their surfaces[21, 22].

The important structural modifications from f-CNTs to CNT/CeO_2 composites are also reflected in the Raman spectra, which corroborates the interaction between CNTs and nano ceria. In Fig. 2b, Raman spectra of f-CNTs display two distinct characteristic bands in the high-frequency region ascribing to the D-band line (about 1341 cm^{-1}) and the G-band line (about 1583 cm^{-1}). The G-band is associated with the vibrations of ordered sp^2 hybridized carbon, while the marked D band is produced by the tangential mode vibrations of local defects and imperfections of sp^3 hybridized carbon. Further, the well resolved CeO_2 Raman peak appeared at 450 cm^{-1} is observed in CeO_2 nanoparticles, which is attributed to the main symmetric vibrations of the Ce–O (F2g) Raman active mode.

Raman spectra of nanocomposite (Fig. 2b) displayed the bands of both CNT and nano CeO_2. The D and G bands of the nanocomposite were slightly shifted, as compared to those of the CNTs. The D band of the composite was shifted to a lower wavenumber by 5 cm^{-1} , whereas the G band showed a red shift of 6 cm^{-1} . Apart from the shift in the peak position, the intensity ratio of the D and G bands (I_D/I_G) of the nanocomposite (1.12) was lower than that of f-CNT (1.84), which was prudently ascribed to the interaction between CeO_2 and $CNTs$[23].

Degradation trends with temperature of pristine CNT, f-CNT, nano ceria and their composites were investigated using TGA and are shown in Fig. 3. Comparing the weight loss in the temperature range 100-500 and 500-800 °C, the maximum weight loss was found to be about 4% for pristine CNTs and 28% in case of f-CNT in the temperature range of 100-500 °C, which probably due to the oxygen functionalities or due to the presence of carboxylic group, thus confirming the acid functionalization on the surface of CNTs. In the case of CNT/CeO_2 nanocomposite, compared with f-CNT there are little improvements in both the first decomposition step between 100 and 150 °C and the second decomposition around 300 °C. The nanocomposite displays a weight loss before 200 °C, corresponding to the elimination of absorbed water. However, it is impossible to extract the exact amount of CNTs from the TGA curve, since the oxidation of nanoceria and CNT are overlapped[17].

3.2 Surface analysis

Surface morphologies of the *f*-CNTs, nano-ceria and CNT/CeO$_2$ observed by SEM are illustrated in Fig. 4 (a-d). It can be seen that *f*-CNTs exhibit a denser network of CNTs with smooth and clean surface prior to the deposition of CeO$_2$ nanoparticles. From the observation of SEM images of CeO$_2$ nanoparticles (Fig. S2), it's obviously showed that synthesized CeO$_2$ nanoparticles exhibited nonsperical morphology with the diameter of about 10–15 nm. Conversely, after the construction of composites, the magnified SEM image, as shown in Fig. 4c, suggests that a large number of nanoparticles are uniformly anchored on the surface of CNTs, confirming the successful deposition of CeO$_2$ nanoparticles on the CNT surface. The energy-dispersive X-ray (EDX) spectrum of CNT/CeO$_2$ (Fig. 4d) reveals the existence of Ce element in synthesized nanocomposite.

Fig. 5a illustrates the TEM image of the pristine CNTs. It can be witnessed that the raw CNTs exhibit a diameter of 10–15 nm and a length of ~ 3 µm with a smooth surface. After treating by acid mixture, the surface of the CNTs turns into rough and the length is considerable reduced (250–300 nm). This modification could improve the dispersion or wetting of CNTs during the synthesis of nanocomposite. The corresponding SAED pattern (Fig. 5c, inset) exhibited two well defined electron diffraction rings, which can be attributed to typical (002) and (100) planes of MWCNTs [21].

A TEM image (Fig. 5d) presented that CeO$_2$ nanoparticles had size in the range of 10–15 nm, which agree well with the XRD results. TEM image of CeO$_2$/CNTs is shown in Fig. 6a, which further confirms that CeO$_2$ nanoparticles are neatly aligned along the length of CNTs. Further, the selected area electron diffraction (SAED) pattern inserted in the image of HR-TEM of the CeO$_2$/CNTs nanocomposite displays the four bright concentric diffraction rings composed of spots, which corresponded to the ((111), (200), (220), and (311) planes of face-center cubic of CeO$_2$ nanoparticles, respectively [23]. Uniform fringes, with an interval of 0.295 nm are also clearly visible in the high resolution image of nanocomposite (Fig 6c) further confirmed the deposition of CeO$_2$ nanoparticles on CNTs. It is noteworthy to indicate that CeO$_2$ nanoparticles are certainly anchored on the surface of CNT. The combination of CeO$_2$ and CNT surface can be ascribed to strong interaction through the functional groups on the surface of CNT walls.

3.3 Water contact angle results

Generally, coatings with more hydrophobic character are certainly more resistant against corrosion in aqueous environments[24]. Hence, a correlation between the wettability of a coating and its anticorrosion performance is typically desired to attain complete information about the coating performance in an aggressive environment. The concept of preparing hydrophobic surfaces that repel water creates huge opportunities in the area of corrosion protection for metals and alloys. Several works have been performed to study the corrosion resistance of metals coated with hydrophobic surfaces [25]. The corrosion resistance mechanism of hydrophobic surfaces proceeds as follows: when exposed to a corrosive medium, hydrophobic coatings, made of hierarchical rough structures can easily trap a large amount of air within the valleys between the rough structures. These ''air valleys'' impede the infiltration of corrosive ions, such as Cl$^-$ [26]. Figure 7 shows the variation of contact

angle values with the CNT/CeO$_2$ nanocomposite and the error bars for each plot mean maximum and minimum water contact angles on the same substrates. The obtained contact angle images from uncoated and coated MS substrates are clearly shown in Fig.S3. It can be seen that the water contact angle increased linearly with increasing CNT nanocomposite amounts. This intends that the microstructure alteration of the coating upon adding the CNT/CeO$_2$ nanocomposite was influenced on the surface roughness that is well-known to offer a hydrophobic effect on the coatings [25,27-29].

3.4 Electrochemical corrosion test

Fig. 8 represents the typical pontiodynamic polarization curves of uncoated and coated MS in the 3.5 wt.% NaCl solution. For convenience of comparison, the values of corrosion potential (E$_{corr}$) and corrosion current density (i$_{corr}$) extracted from these curves are displayed in Table 1. Compared to uncoated MS, a substantial positively shifted E$_{corr}$ was obtained in all the coated MS, confirming an effective protection of MS against corrosion by the coating [30]. It can be obviously seen that the PU-CNT coatings normally had nobler shift in potential than pure PU coatings in which PU-CNT/Ce2 composite coating had the noblest shift in comparison to other coatings. Furthermore, i$_{corr}$ value of nanocomposite coatings has fairly diminished; the lowest value of i$_{corr}$ for PU-CNT/Ce2 coating is almost 50 times lower than that of the pure PU coating. A much lower corrosion current density (12.15 × 10^{-3} μA/cm^2) and a higher corrosion potential (−342 mV) could be noticed for the PU-CNT/Ce2. This inferred that the effective sealing presented by the nanocomposite coatings circumvents the penetration of corrosive ions through the pores and cracks and improved the corrosion resistance of the PU coating.

The Bode plots of uncoated and coated MS in the 3.5 wt.% NaCl solution are presented in Fig. 9. Coated MS substrates exhibit a different response in the Bode plots when compared with the uncoated MS. In general, the overall corrosion protection conferred by the coatings could be investigated through the evaluation of the low-frequency domain of impedance spectra [31]. The impedance modulus at the low frequency domain (Z$_{mod}$ at 0.01 Hz) is one of the parameters which can be certainly employed to relate the corrosion resistance of different samples. In the present investigation, low frequency impedance values in the range of 10^6–10^7 Ω cm^2 are observed for nanocomposite coating, which is greater than uncoated and other coatings, thus confirming the enhanced corrosion protection offered by them.

The electrochemical behavior can be designated in terms of an equivalent circuit in order to assist the most relevant parameters appropriate to the corroding system to be acquired. Equivalent circuits used for fitting EIS data are shown as supplementary information in Fig. S4. To attain a satisfactory impedance simulation, it is essential to replace the capacitor (C) with a constant phase element (CPE) Q in the equivalent circuit. Constant phase element Q$_1$, Q$_2$, Rs, R$_f$ and R$_{ct}$ can be corresponded to double layer and coating layer capacitance, solution resistance film resistance and charge transfer resistance, respectively. It can be seen that the charge transfer resistance (R$_{ct}$) in PU composites coatings is higher than that in pure PU, which means the presence of CNT/CeO$_2$ surely has enhanced the corrosion resistance of PU coating. The results imply that increasing the amount of CNT/CeO$_2$ up to 1wt. % offer an increase in R$_{ct}$ value, which imply on better corrosion resistance

due to the inclusion of synthesized nanocomposites. However, in the amount of 2 wt.% of CNT/CeO$_2$ in PU coatings, R$_{ct}$ slightly decreased which could be due to a heterogeneous microstructure, originating from nonuniform dispersion of CNT/CeO$_2$ particles in PU coating. This inhomogeneity in PU coating could also be supported by means of the parameter n. The value of n ascribed to the linear slope modulus of the Bode plot and it is already reported that the surface is uniform and smooth when n is near 1[32]. Simultaneously, lower values (Herein, n = 0.712 in PU-CNT/Ce3) illustrates deviation from ideal capacitive behavior (which has been attributed to the inhomogeneity of the surface) and weakening in corrosion resistance. The EIS data is in good agreement with polarization results, representing that the best protection was offered by PU-CNT/Ce2 coatings. Fig. S5 shows the SEM images for uncoated and coated MS substrates after corrosion test. As expected, corrosion occurred and rust formed and distributed uniformly over the exposed area of the uncoated MS substrate. For the MS substrates with PU and PU/CNT coating, displayed less cracked areas and showed a more uniform surface without any sign of peeling on their surfaces. Finally, the PU coating with 1 wt% of nanocomposites showed no sign of corrosion, which confirms the excellent corrosion protection for MS by the PU-CNT/Ce2. Based on the electrochemical corrosion results, the corrosion protection performance of the uncoated and coated MS substrates is ranked as follows: PU-CNT/Ce2 > PU-CNT/Ce3 > PU-CNT/Ce1 > PU-CNT > PU > Uncoated.

Conclusions

CNT/CeO$_2$ nanocomposite was successfully synthesized and the characterization of the materials demonstrated that the CeO$_2$ nanoparticles with several nanometers in size were tightly anchored on CNT surface. IR and UV spectral studies revealed the interaction between the CeO$_2$ nanoparticles and the carboxylic groups in the wall of the CNT surface. Lower I$_D$/I$_G$ of the nanocomposite in Raman spectra reasonably confirmed the interaction between CeO$_2$ and CNTs. Water contact angle increased linearly with increasing CNT nanocomposite amounts in the coatings further support the enhanced corrosion performance on MS surface. It is evident from the electrochemical studies that the hybrid composite coatings developed with CNT/CeO$_2$ in optimum concentration in the PU matrix revealed better corrosion protection in 3.5% NaCl than that of the coatings developed without it. Hence, it is anticipated that the CeO$_2$/CNT nanocomposite will have a promising potential for application in surface protective coatings.

Acknowledgement

Reference

[1] Dimitriya Borisova, Helmuth Möhwald, Dmitry G. Shchukin, *ACS Nano,* 2011, 5, 1939–1946.

[2] A.C. Balaskas, I.A. Kartsonakis, L.A. Tzivelekaa, G.C. Kordas, *Progress in Organic Coatings,* 2012, 74, 418–426.

[3] F. Ansari, R. Naderi, C. Dehghanian, *RSC Advances*, 2015, 5, 706–716.

[4] Uday Narayan Maiti, Won Jun Lee, Ju Min Lee, Youngtak Oh, Ju Young Kim, Ji Eun Kim, Jongwon Shim, Tae Hee Han, Sang Ouk Kim, *Advanced Material,* 2013, 26, 40–67.

[5] Vasilios Georgakilas, Dimitrios Gournis, Vasilios Tzitzios, Lucia Pasquato, Dirk M. Guldie, Maurizio Prato, *Journal of Materials Chemistry*, 2007,17,2679–2694.

[6] Cedric Bouzigues, Thierry Gacoin, Antigoni Alexandrou, *ACS Nano,* 2011, 5, 8488–8505.

[7] X. Li, L. Sun, A. Ge, Y. Guo, *Chemical Communications,* 2011, 47, 947–949.

[8] N. Selvakumar, K. Jeyasubramanian, R. Sharmila, *Progress in Organic Coatings,* 2012,74,461–469

[9] M. Fedel, A. Ahniyaz, L. G. Ecco, F. Deflorian, *Electrochimica Acta*, 2014, 131, 71-78

[10] Gia Vu Pham, Anh Truc Trinh, Thi Xuan Hang To, Thuy Duong Nguyen,Thu Trang Nguyen, Xuan Hoan Nguyen, *Advanced Nature Science: Nanoscience Nanotechnology,* 2014, 5, 035016.

[11] X.H. Chen, C.S. Chen, H.N. Xiao, F.Q. Cheng, G. Zhang, G.J. Yi, *Surface and Coatings Technology,* 2005,191, 351–356.

[12] B.M. Praveen, T.V. Venkatesh, Y. Arthoba Naik, K. Prashanth, *Surface and Coatings Technology*, 2007, 201, 5836–5842.

[13] Huige Wei, Daowei Ding, Suying Wei, Zhanhu Guo, *Journal of Materials Chemistry A*, 2013,1,10805- 10813.

[14] S.A.R. Hashmi, Harish Chandra Prasad, R. Abishera, Hari Narayan Bhargaw, Ajay Naik, *Materials and Design* 2015,67,492–500.

[15] M. Abdel Salam, S.S. Al-Juaid, A.H. Qusti, A.A. Hermas, *Synthetic Metal,* 2011,161, 153–157

[16] Dengsong Zhanga, Hailing Mai, Lei Huang, Liyi Shi, *Applied Surface Science,* 2010, 256, 6795–6800.

[17] Minori Taguchi, Seiichi Takami, Tadafumi Adschiri, Takayuki Nakane, Koichi Sato, Takashi Naka, *Crystal Engineering Communications*, 2011, 13, 2841-2848.

[18] Y. Sasikumar, A. Madhan Kumar, Zuhair M.Gasem, Eno E.Enbenso, *Applied Surface Science,* 2015, 330, 207–215.

[19] V. C. Tung, L. M. Chen, M. J. Allen, J. K. Wassei, K. Nelson, R. B. Kaner, Y. Yang, *Nano Letters,* 2009, 9, 1949–1955.

[20] Xue Jiao, Hongjie Song, Huihui Zhao, Wei Bai, Lichun Zhang, Yi Lv, *Analytical Methods*, 2012,4,3261-3267.

[21] Hui Xia, Yu Wang, Jianyi Lin and Li Lu, *Nanoscale Research Letters*, 2012, 33, 1-10

[22] B. P. Vinayan, Rupali Nagar, V Raman, N Rajalakshmi, K.S. Dhathathreyan, S Ramaprabhu, *Journal of Materials Chemistry*, 2012,22, 9949-9956.

[23] N. Padmanathan, S. Selladurai, *RSC Advances,* 2014, 4, 6527-6534.

[24] P. Wang, D. Zhang, R. Qiu, Y. Wan, J. Wu, *Corrosion Science,* 2014,80, 366–373

[25] Adel M.A. Mohamed, Aboubakr M. Abdullah, Nathalie A. Younan, *Arabian Journal of Chemistry,* doi:10.1016/j.arabjc.2014.03.006.

[26] Wenji Xu, Jinlong Song, Jing Sun, Yao Lu, and Ziyuan Yu, *ACS Applied Materials Interfaces*,2011,1, 4404–4414.

[27] Jinlong Song, Wenji Xu, Yao Lu, Xin Liu, Zefei Wei, Jing Sun, *Micro Nano Letters*, 2012, 7, 204 – 207.

[28] A. Madhankumar, Zuhair M. Gasem, *Progress in Organic Coatings*, 2015, 78,387–394.

[29] Ishizaki, T., Masuda, Y., Sakamoto, M., *Langmuir* 2011, 27, 4780–4788.

[30] A. Madhan Kumar, R. Suresh babu, I.B. Obot, Zuhair M. Gasem, *RSC Advances*, 2015,5,19264–19272.

[31] A. Madhankumar, Elangovan Thangavel, Suresh Ramakrishna, I.B.Obot, Hwa Chul Jung, Kwang Seon Shin, Zuhair M.Gasem, Hyongbum Kim, Dae-Eun Kim, *RSC Advances*, 2014,4,24272–24285.

[32] A. Madhankumar, S. Nagarajan, N. Rajendran, T. Nishimura, *Journal of Solid State Electrochemistry*, 2012, 16, 2085-93.

Figure captions

Figure 1 (a) IR and (b) UV absorbance curves of f-CNTs, synthesized CeO_2 nanoparticles and CNT/CeO_2 nanocomposite

Figure 2 (a) XRD and (b) Raman spectra of f-CNTs, synthesized CeO_2 nanoparticles and CNT/CeO_2 nanocomposite

Figure 3 TGA curves of f-CNTs, synthesized nano-CeO_2 and CNT/CeO_2 nanocomposite

Figure 4 SEM images of (a) f-CNTs (b) CNT/CeO_2 nanocomposite (low magnification) and (c) CNT/CeO_2 nanocomposite (high magnification) and (d) EDX results of nanocomposite

Figure 5 TEM images of (a) pristine CNTs (b) f-CNTs, (c) f-CNTs (high magnification) (d) CeO_2 nanoparticles

Figure 6 TEM images of (a) CNT/CeO_2 nanocomposite (low magnification) (b) CNT/CeO_2 nanocomposite (high magnification) and (c) High resolution image of CNT/CeO_2 nanocomposite and (d) d-spacing line profile

Figure 7 Contact angle results of uncoated and coated MS substrates

Figure 8 Potentiodynamic polarization curves of uncoated and coated MS substrates

Figure 9 Bode plots of uncoated and coated MS substrates

Table captions

Table 1 Tafel plot parameters of uncoated and coated MS substrates.

Table 2 EIS parameters of uncoated and coated MS substrates.

Figure 1
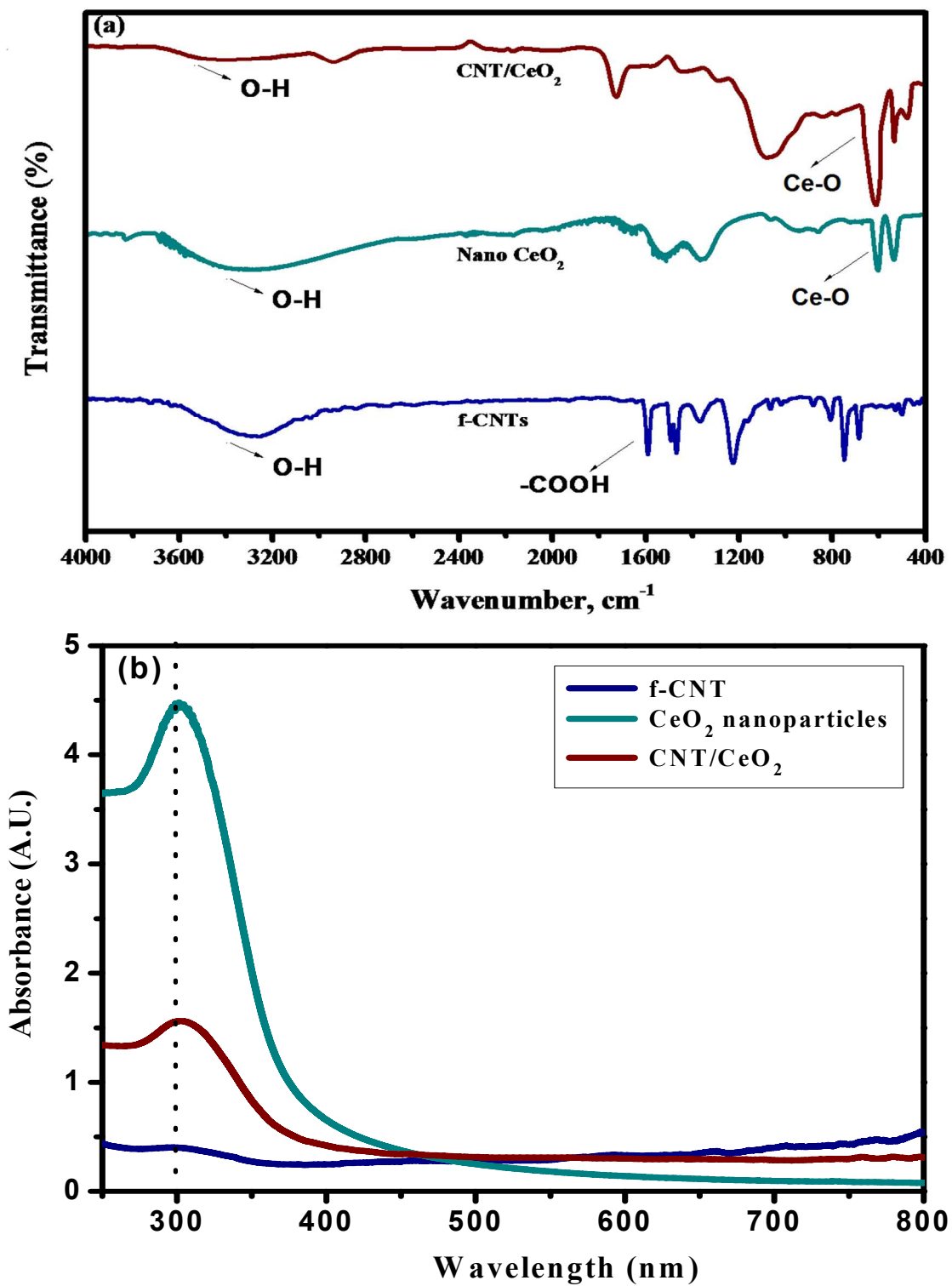
Figure 2
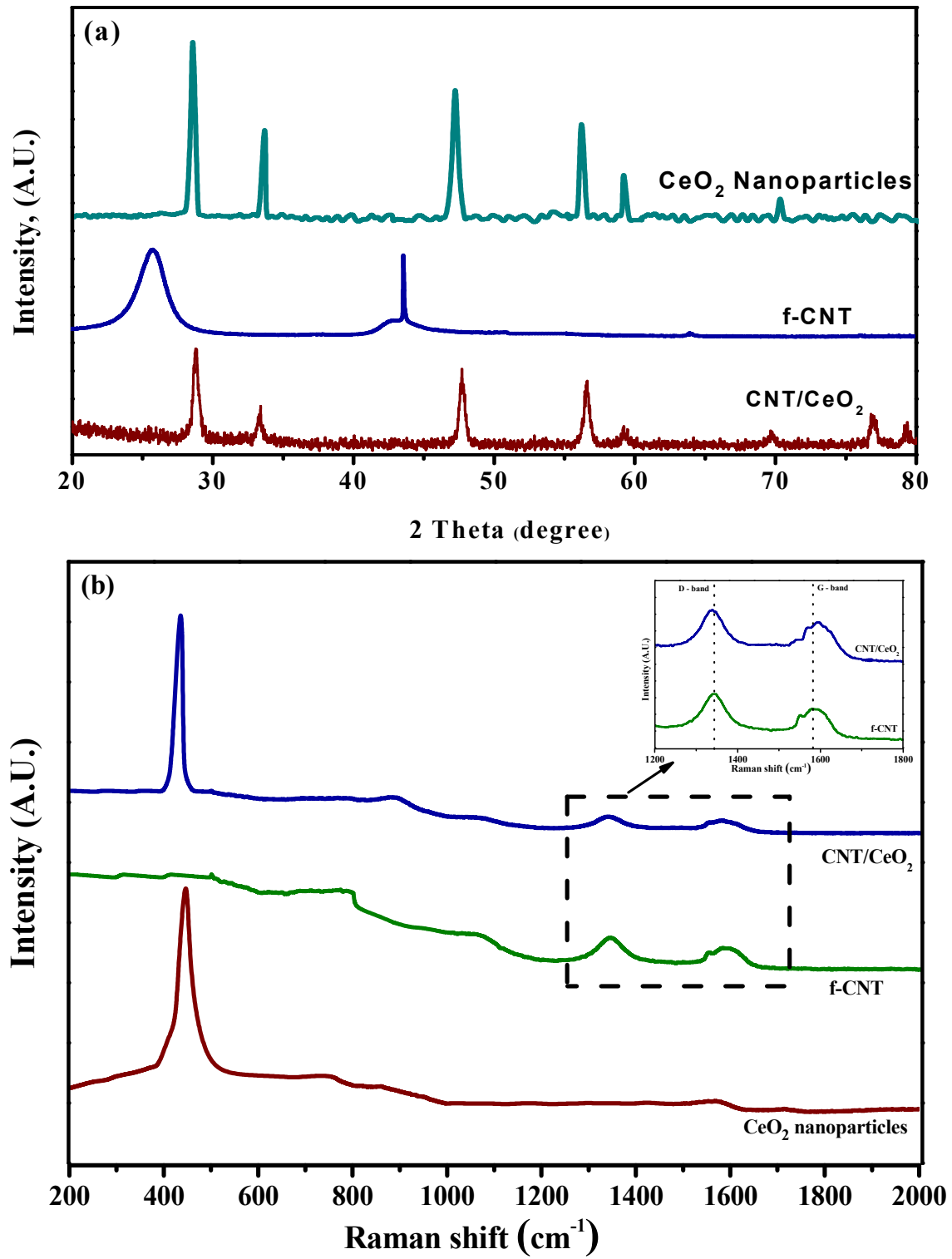
Figure 3
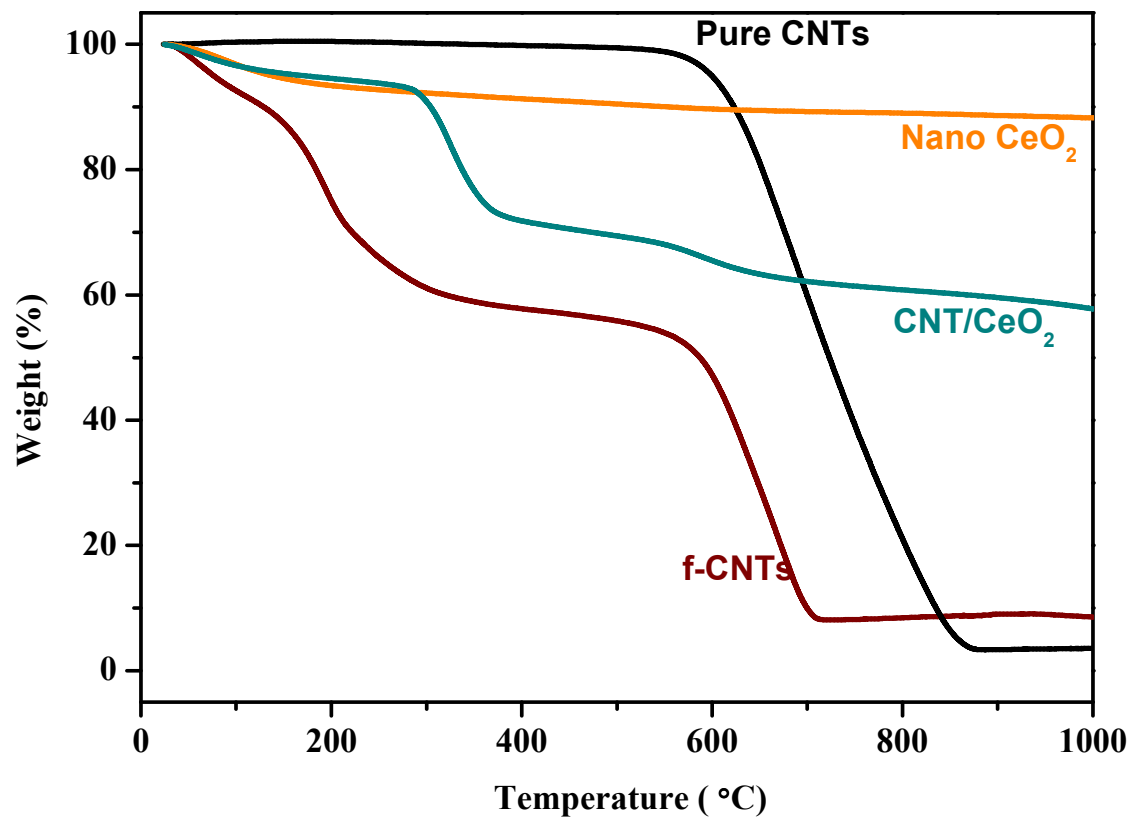
Figure 4
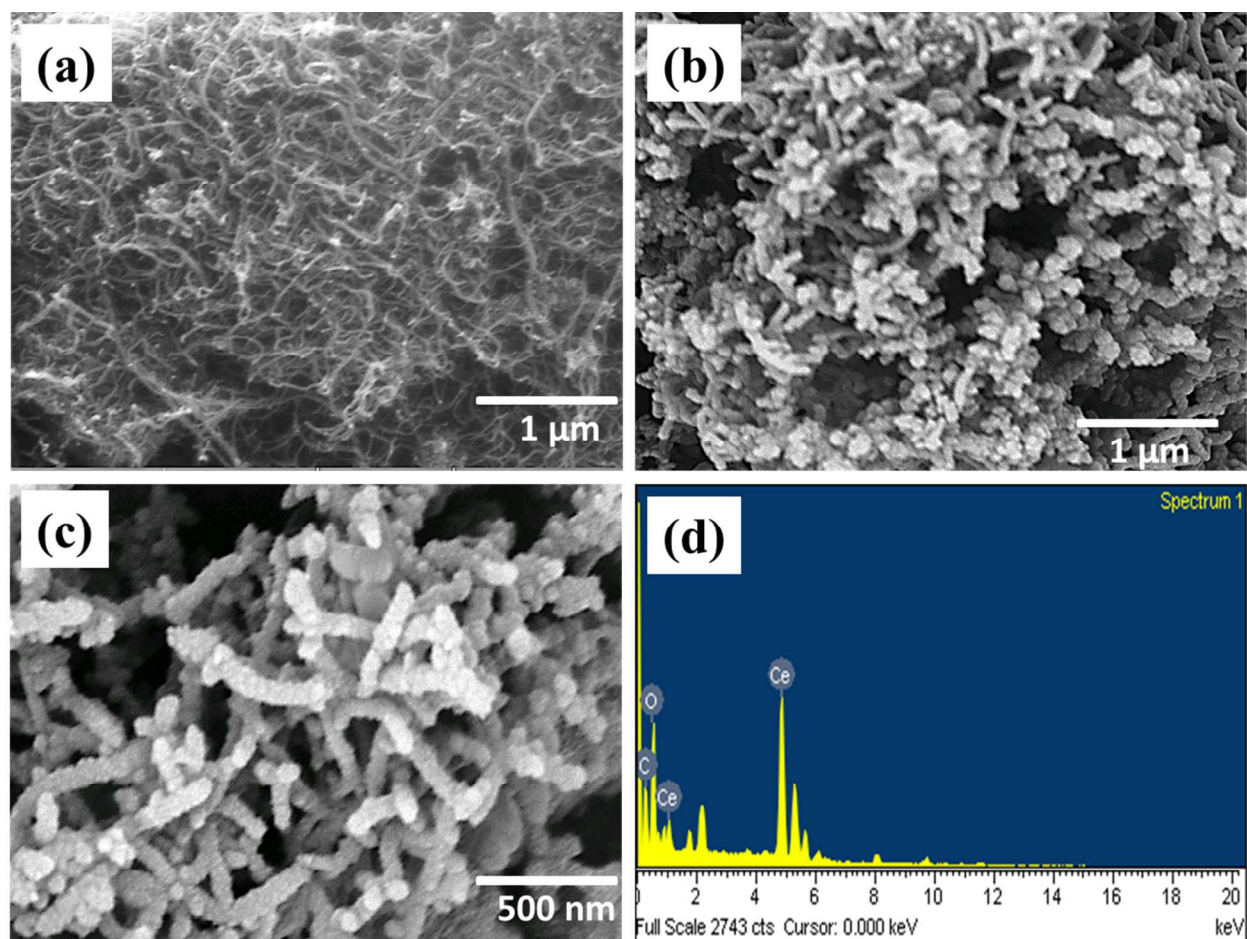
Figure 5
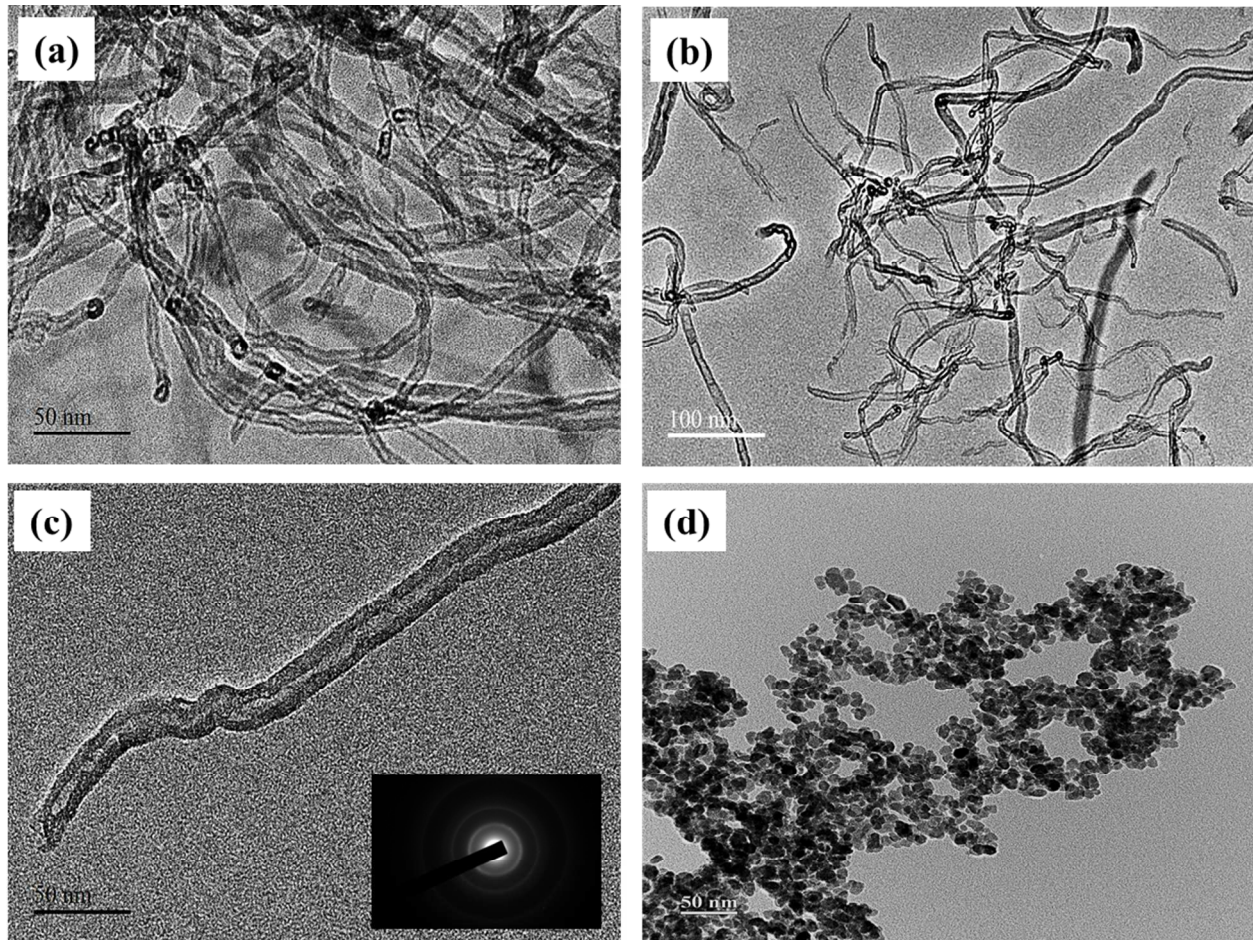
Figure 6
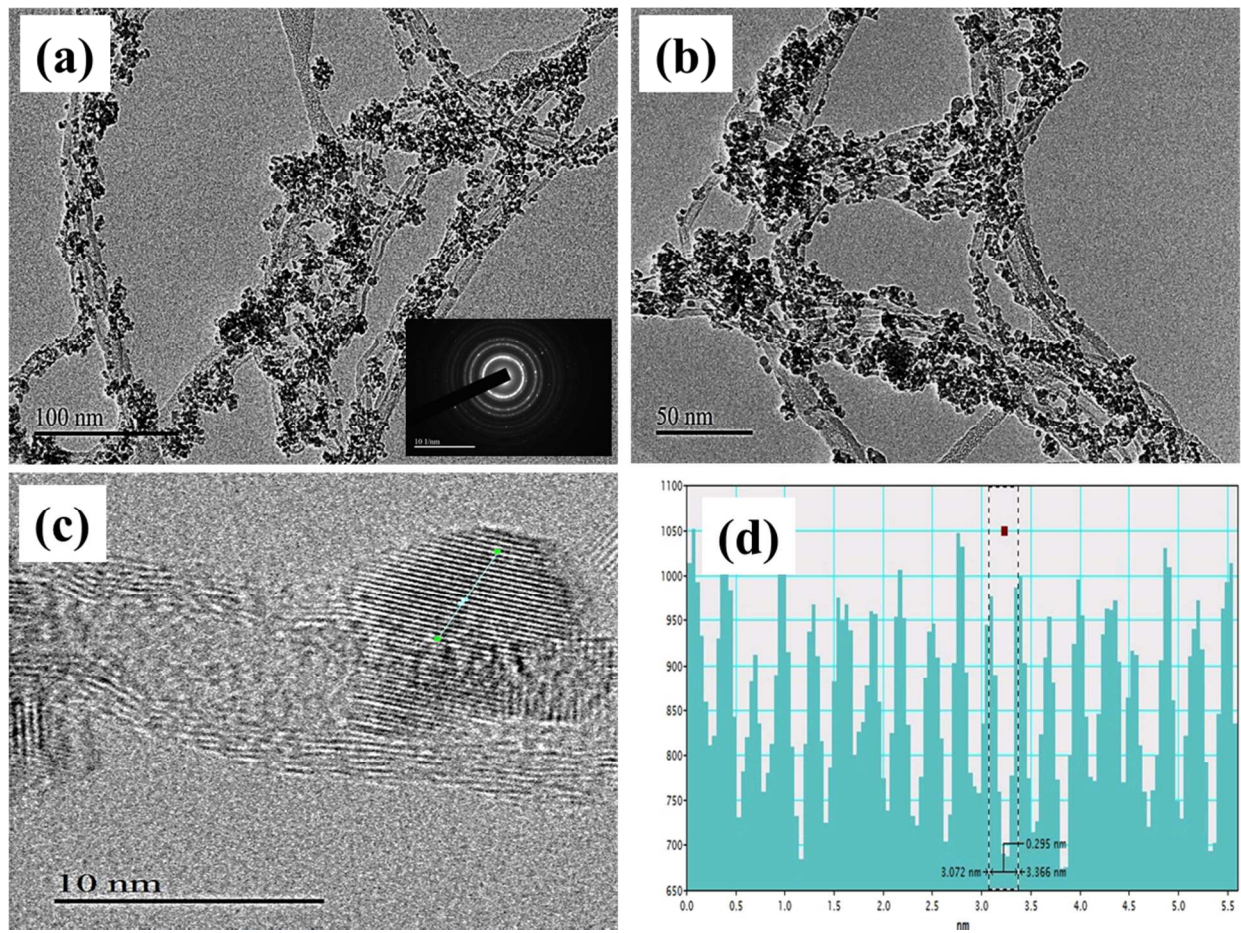
Figure 7
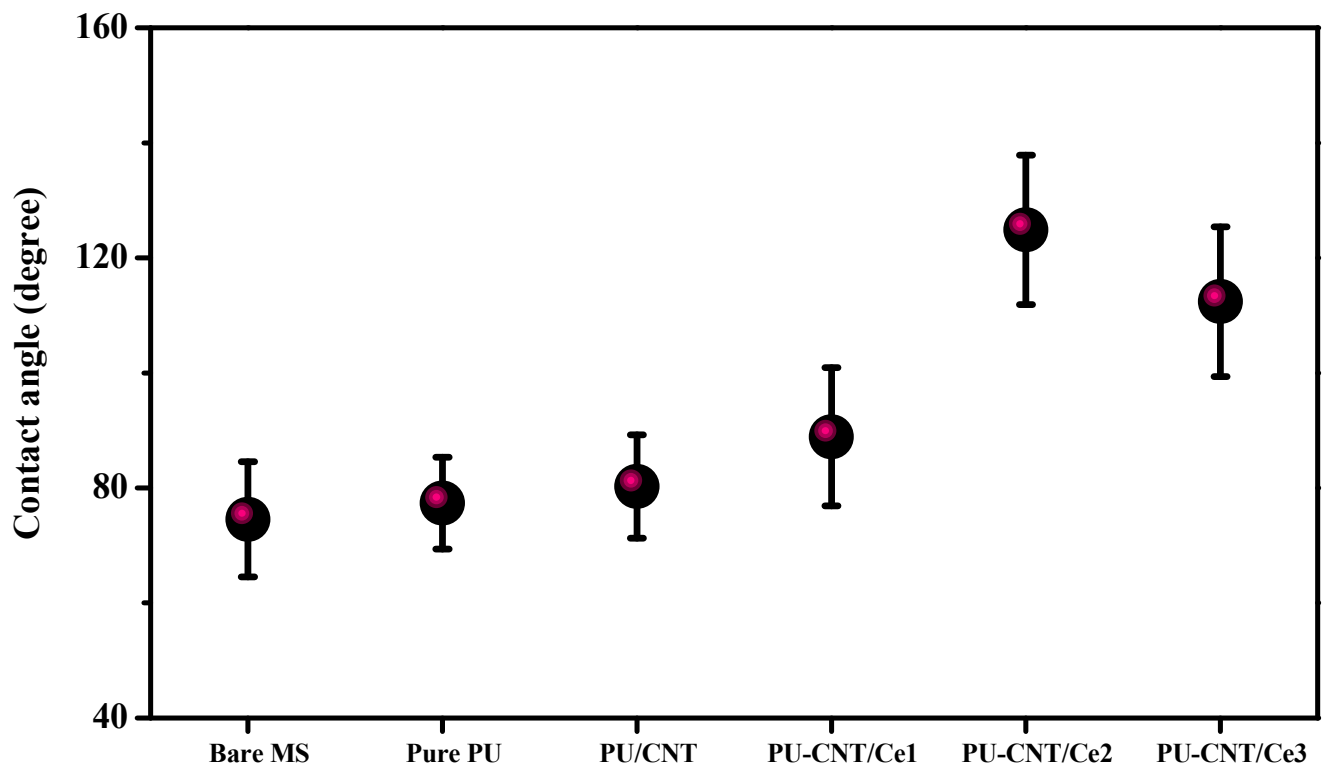
Figure 8
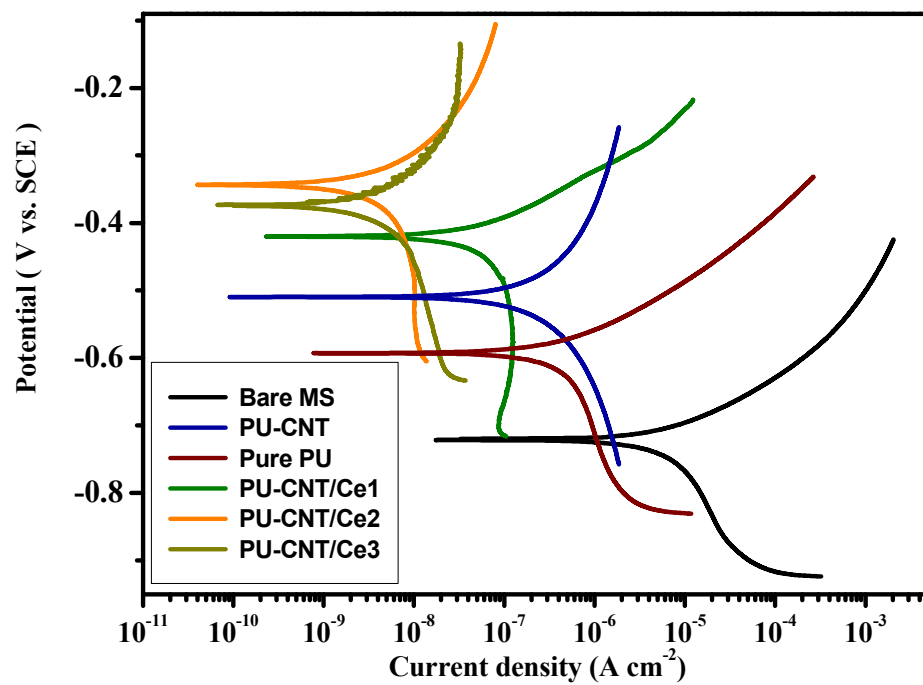
Figure 9
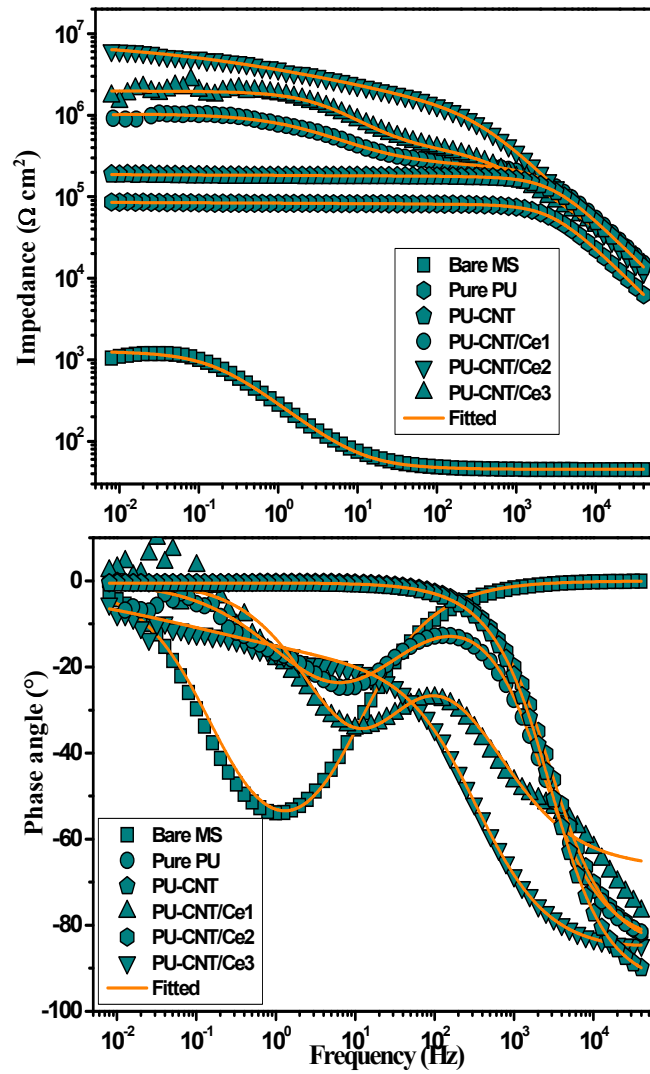
Table 1

S. No.	Substrate	E_{corr} mV	I_{corr} $\mu A\ cm^2$	βa mV/dec	β_b mV/dec	Corr. Rate (mpy)
1	Uncoated	-721	4.3801	100	169	2.5383
2	PU	-593	0.6984	96	137	0.4058
3	PU-CNT	-510	0.5003	71	62	0.0125
4	PU-CNT/Ce1	-420	0.1197	96	73	0.0610
5	PU-CNT/Ce2	-342	0.0121	176	163	0.0071
6	PU-CNT/Ce3	-376	0.0293	95	114	0.0171

Table 2

S. No	Substrate	R_s Ω cm^2	R_{ct} kΩ cm^2	Q_{dl} μF cm^{-2}	n	R_f kΩ cm^2	Q_f μF cm^{-2}	n
1	Uncoated	45.22	1.22	787.65	0.82	------	------	-----
2	PU	56.21	134.81	431.21	0.87	120	68.38	0.85
3	PU-CNT	52.34	180.32	2.90	0.91	169	43.46	0.90
4	PU-Ce/CNT1	48.35	918.32	0.22	0.94	238	23.62	0.93
5	PU-Ce/CNT2	57.59	6228.00	0.04	0.93	437	6.33	0.97
6	PU-Ce/CNT3	87.59	2188.00	0.14	0.90	637	16.22	0.93